ISSN 0015-4628, Fluid Dynamics, 2022, Vol. 57, Suppl. 1, pp. S97–S116. © Pleiades Publishing, Ltd., 2022.

Numerical Simulation of Shock-Wave Interaction with a Laminar Boundary Layer in a Hypersonic Flow around Models with a Kink in the Generatrix

S. T. Surzhikov[a,b,*]

[a] *Ishlinsky Institute for Problems in Mechanics, Russian Academy of Sciences, Moscow, 119526 Russia*

[b] *All-Russian Research Institute of Automation, Moscow, 127030 Russia*

**e-mail: surg@ipmnet.ru*

Received July 11, 2020; revised July 18, 2022; accepted July 18, 2022

Abstract—A series of experimental data obtained at the Calspan–University at Buffalo Research Center (CUBRC) and accompanying numerical calculations performed by members of the computer code testing working group were used to validate the author's PERAT-2D computer code. The problems of a hypersonic flow of molecular nitrogen around a sharp and blunt cone with a kink in the generatrix, as well as around a hollow cylinder with a sharp edge and an expanding skirt, are considered.

Keywords: hypersonic flow, interaction of a shock wave with a boundary layer, validation of author's computer code

DOI: 10.1134/S001546282260122X

1. INTRODUCTION

The experimental data base obtained at the Calspan–University at Buffalo Research Center (CUBRC) in the course of studying the features of hypersonic flows around axisymmetric models with a kink of the generatrix was used as a basis for validating calculations within a specially organized working group for comparing the calculated and experimental data [1–19]. Similar studies were carried out in parallel by other scientific groups [20–28]. The results of detailed experimental and computational studies carried out at the Central Aerodynamic Institute under the supervision of V.Ya. Borovoy are given in monograph [26].

A part of the full matrix of experimental data used for the validation of computer codes is presented in Table 1. For some experimental points, there are several options for the initial data. According to [2], some of these data were refined in experiments and some of the data correspond to the calculated prediction of parameters of the oncoming flow, also taking into account nonequilibrium physicochemical processes.

A detailed analysis of these experimental data and the results of a computational study revealed several fundamental features of the shock-wave interaction with the laminar boundary layer, as well as the development of the separation zone towards the flow in the vicinity of the kink of the generatrix of the model under study.

One of the important results concerning the numerical simulation of these problems was the conclusion about the extreme sensitivity of the calculated data to the quality of the calculation method and the degree of detail of the calculation grids used. In particular, in [3], these problems were solved using the WIND (NPARC Alliance) and DPLR (NASA Ames Research Center) codes. The experimental data for two aerodynamic models for testing were as follows: a hollow cylinder with a skirt expanding at an angle of 30° and a double cone with opening angles of 25° and 55°. One of the cones was sharp, and the second had a rounding radius of 0.635 cm. The calculations were carried out on the same structured computational grids of different detail (for example, for a double cone: 128 × 48, 256 × 96, 512 × 192, 1024 × 384, and 2048 × 768).

Table 1. Initial data of hypersonic flow tests

Run #	V_∞, cm/s	ρ_∞, g/cm^3	p_∞, erg/cm^3	T_∞, K	M	References
11a	2.609×10^5	0.5066×10^{-6}	194	128.9	11.1	[2, 9]
11b	2.485×10^5	0.5866×10^{-6}	171.9	98.7	12.3	[2]
14a	2.432×10^5	0.7937×10^{-6}	367.9	156.1	9.5	[2, 9]
14b	2.327×10^5	0.7506×10^{-6}	254.3	114.19	10.7	[2]
14c	2.304×10^5	0.8810×10^{-6}	318.8	120.4	10.3	[3]
24	2.614×10^5	1.3700×10^{-6}	619	152.	10.4	[1]
28a	2.522×10^5	0.7267×10^{-6}	299.9	139.	10.5	[1]
28b	2.664×10^5	0.6345×10^{-6}	360.6	185.6	9.59	[2, 9]
28c	2.538×10^5	0.7372×10^{-6}	306.4	140.	10.5	[2]
35a	2.577×10^5	0.6082×10^{-6}	185.5	102.7	12.5	[1]
35b	2.713×10^5	0.5515×10^{-6}	227.4	138.9	11.3	[2, 9]
31	2.623×10^5	0.5670×10^{-6}	180.6	107.3	12.4	[3]
32	2.574×10^5	0.7576×10^{-6}	320.6	142.5	10.6	[1]
36	2.586×10^5	1.1080×10^{-6}	495.8	150.7	10.3	[1]

In addition to the mathematical estimation of the accuracy of the numerical results using the computational technology with a sequence of computational grids, in [3], the data obtained were compared in terms of pressure and heat transfer (Stanton coefficient) coefficients

$$C_p = \frac{p - p_\infty}{0.5\rho_\infty V_\infty^2},$$

$$C_h = \mathrm{St} = \frac{q_w}{0.5\rho_\infty V_\infty^3},$$

where p and q_w are the pressure and density of the convective heat flux on the surface of the body and p_∞, ρ_∞, and V_∞ are the pressure, density, and velocity of the oncoming flow.

The calculation codes mentioned above showed fairly close results. However, the use of different computational grids led to qualitatively different data.

The aerodynamic models studied proved to be very convenient for obtaining visual qualitative and quantitative experimental data on the shock-wave interaction with the boundary layer. The computational domains and highly sparse grids used in this study are shown in Fig. 1.

In experiments, both in the flow around a hollow cylinder with pointed edges and a skirt and around a double cone, four characteristic flow regions near the surface were revealed. For example, Fig. 2 shows the distributions of coefficients C_p and $C_h = \mathrm{St}$ along the surface of a double blunt cone (see Fig. 1c). The first region corresponds to the flow around a spherical bluntness, turning into a cone with an opening angle of 25°.

In the second zone, there is an increase in pressure and a decrease in the density of the convective heat flux in the zone of separated flow in front of and above the kink of the generatrix. The third zone, the zone of maximum growth of C_p and C_h, corresponds to the position of the fall of the outgoing bow shock wave onto the boundary layer. The fourth zone corresponds to the pressure and heat transfer behind the place where the shock wave interacts with the boundary layer.

It was found that the most important indicator of the quality of the solution obtained is the accuracy of numerical prediction of the separation zone length, the location of the region of interaction of the shock wave with the boundary layer, and the absolute values of coefficients C_p and C_h in these zones. The most sensitive to the computational grids was the calculated length of the separation zone and the values of coefficients C_p and C_h in it.

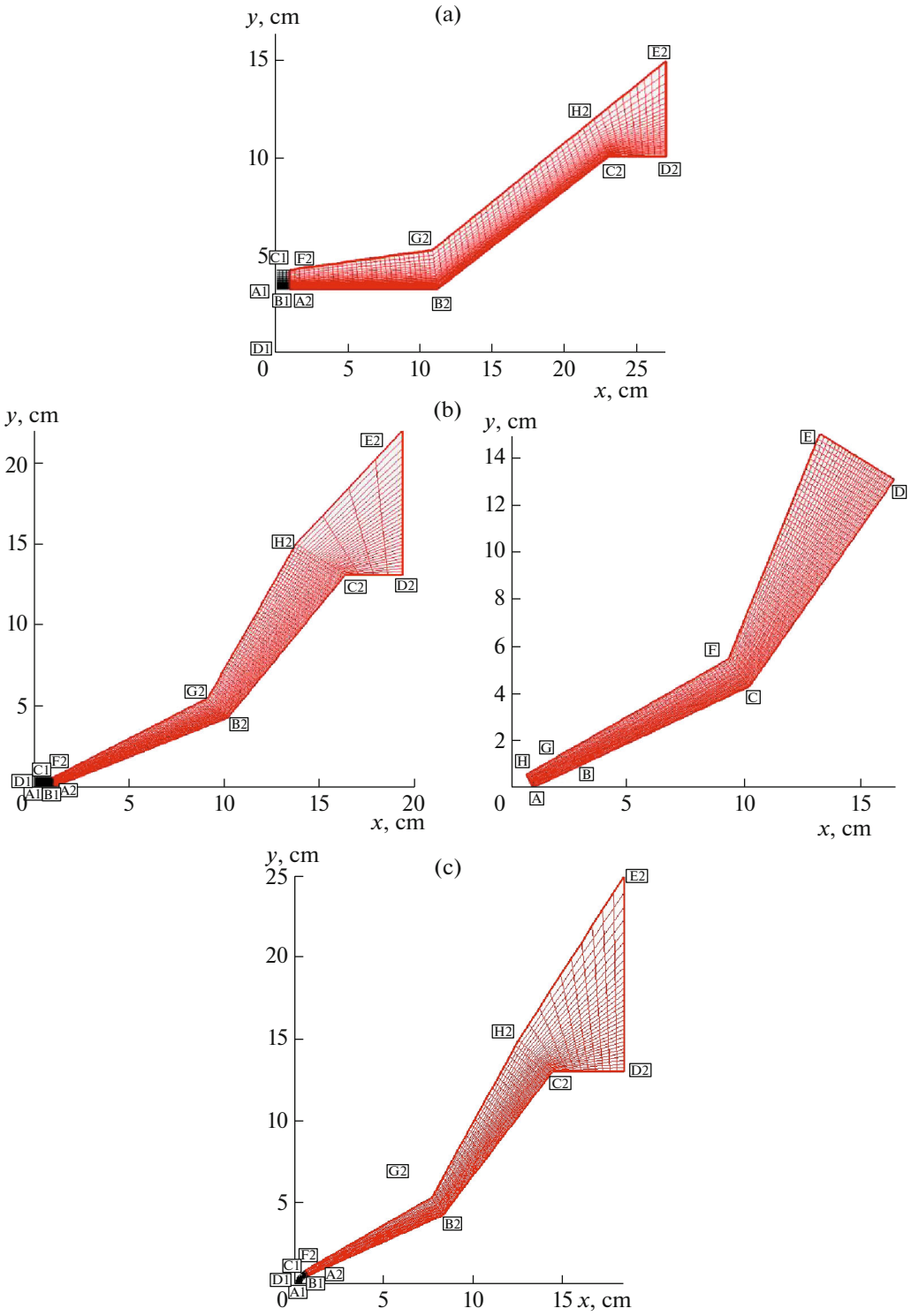

Fig. 1. Geometry and computational domain of a (a) hollow skirted cylinder, (b) double sharp cone, and (c) double blunt cone.

In [3], calculations were performed using the DPLR code not only using the perfect gas model, but also taking into account nonequilibrium physicochemical processes. Some non-fundamentally important effects on the calculation results were shown. The use of DSMC calculation codes gave a more noticeable discrepancy with the experimental data, which was the subject of a detailed analysis in [1, 2].

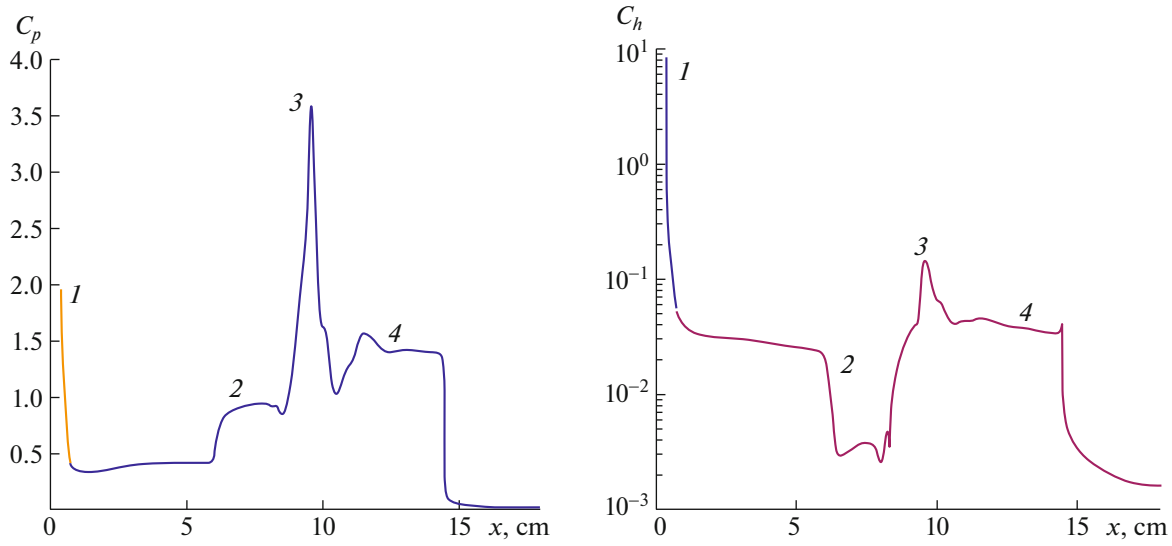

Fig. 2. Characteristic elements of surface distributions of pressure (C_p) and heat (C_h) transfer coefficients in a hypersonic flow around models.

The results of the experimental study of hypersonic flows and the validation of computer codes supported by the CUBRC and the Air Force Office of Scientific Research (AFOSR) are summarized in [1].

Significant efforts have been made to reliably determine the flow parameters on tested models. In this study, a detailed analysis of each experimental test and the corresponding validating calculations is given. An analysis of the calculated data presented in [5–12] is also given.

As already noted, a generally good agreement between the calculated and experimental data was demonstrated. At the same time, the analysis of the results of calculations by different authors shows that the same codes do not always give full agreement with the experiment. Here, it should be especially noted that the reliability of the experimental data in this case is not in doubt. First, it is noteworthy that the conducting of these experiments was done with high thoroughness [1]. Secondly, a series of validation calculations by different authors, also performed with great care, confirm the de facto correspondence of the experimental data obtained to the initial data used in the oncoming flow and to the geometric parameters of the models [13–15]. Nevertheless, the efforts made to validate computer codes on the CUBRC experiments as examples led to some refinement of the experimental data [2]. For example, the analysis of the Run#11 experiment revealed very good agreement with the experiment in the separated flow region of the calculated data of Kato and Tannehill [8]. In this case, the calculations of Candler [9] and Gnoffo [10] give a more extended separation zone. At the same time, the calculations of Candler and Gnoffo are in perfect agreement with the Run#28 experimental data.

Below, using the analysis of the calculation results of this study as an example, it will be shown that these discrepancies may well be due to differences in the topology of the grids used, which once again confirms the high sensitivity of the calculated data to the method used and finite-difference grids.

2. TWO-DIMENSIONAL NUMERICAL NAVIER–STOKES MODELS OF A LAMINAR HYPERSONIC FLOW OF A PERFECT GAS AROUND AERODYNAMIC MODELS. PERAT-2D COMPUTER CODE

The calculation model of a viscous heat-conducting perfect gas is based on the continuity equation, the system of Navier–Stokes equations, the energy conservation equation, and the Claipeyron thermal equation of state for an ideal gas:

$$\frac{\partial \rho}{\partial t} + \operatorname{div}(\rho \mathbf{V}) = 0, \tag{2.1}$$

$$\frac{\partial \rho u}{\partial t} + \operatorname{div}(\rho u \mathbf{V}) = -\frac{\partial p}{\partial x} - \frac{2}{3}\frac{\partial}{\partial x}(\mu \operatorname{div}\mathbf{V}) + \frac{\partial}{\partial y}\left[\mu\left(\frac{\partial u}{\partial y} + \frac{\partial v}{\partial x}\right)\right] + 2\frac{\partial}{\partial x}\left(\mu\frac{\partial u}{\partial x}\right), \tag{2.2}$$

$$\frac{\partial \rho v}{\partial t} + \operatorname{div}(\rho v \mathbf{V}) = -\frac{\partial p}{\partial y} - \frac{2}{3}\frac{\partial}{\partial y}(\mu \operatorname{div}\mathbf{V}) + \frac{\partial}{\partial x}\left[\mu\left(\frac{\partial u}{\partial y} + \frac{\partial v}{\partial x}\right)\right] + 2\frac{\partial}{\partial y}\left(\mu\frac{\partial v}{\partial y}\right), \tag{2.3}$$

$$\rho c_p \frac{\partial T}{\partial t} + \rho c_p \mathbf{V}\operatorname{grad} T = \frac{\partial p}{\partial t} + \mathbf{V}\operatorname{grad} p + \operatorname{div}(\lambda \operatorname{grad} T), \tag{2.4}$$

where x, y are Cartesian coordinates, $\mathbf{V} = (u, v)$ is the flow velocity and its projections on the x- and y-axes, ρ and p are the density and pressure, μ is the dynamic viscosity coefficient; c_p is the specific heat capacity at constant pressure, T is temperature, and λ is the thermal conductivity. The energy conservation equation is written here in a nonconservative form with respect to temperature (in the form of the Fourier–Kirchhoff equation).

System of equations (1)–(4) is used together with the equation of state of an ideal gas:

$$p = \rho \frac{R_0}{M_\Sigma} T, \tag{2.5}$$

where $R_0 = 8.314 \times 10^7$ erg/(mol K) is the universal gas constant and $M_\Sigma = 29$ g/mol is the molecular weight of the gas.

Boundary conditions define the unperturbed oncoming flow (see Fig. 1):

$$s(x, y):\ u = u_\infty,\quad v = 0,\quad T = T_\infty,\quad p = p_\infty,\quad \rho = \rho_\infty \tag{2.6}$$

and conditions of the second kind for variation of the functions along flow coordinate ξ are imposed at the exit from the computational domain:

$$x = L: \qquad \frac{\partial u}{\partial \xi} = \frac{\partial v}{\partial \xi} = \frac{\partial T}{\partial \xi} = \frac{\partial \rho}{\partial \xi} = 0. \tag{2.7}$$

On the surface of the body, no-slip conditions are imposed:

$$\eta = 0: \qquad u = v = 0, \quad T = T_w, \quad \frac{\partial p}{\partial \eta} = 0, \tag{2.8}$$

where η is the coordinate line normal to the surface.

This computational model, implemented in the PERAT-2D computer code, is a simplified version of the model on the basis of which the NERAT-2D computer code was created, which has passed a large a series of testing on problems of nonequilibrium aerophysics [29].

Three versions of the PERAT-2D code have been algorithmically implemented:

1) PERAT-2D-2BL two-block computation code without the possibility of automatic grid doubling. The maximum size of computational grids reached 703 × 33 (block 1) + 703 × 1505 (block 2).

2) PERAT-2D-1BL single-block computation code with automatic doubling of the computational grid. The maximum achieved size of the computational grid is 4001 × 385.

3) PERAT-D2D-1BL single-block computation code with double precision and automatic grid doubling.

All computer codes include built-in programs for constructing computational grids with an arbitrary degree of refinement to the surface. No additional refinement in the shock wave region was used.

As in [3], the calculations of each variant were performed on a sequence of computational grids. When using the PERAT-2D-2BL code, the calculations were performed without using multigrid technology.

After obtaining a solution on a given grid, the degree of refinement near the surface was varied. An additional numerical study was carried out with a change in the coordinates of the corner points B2 and G2 (Fig. 1a), B2, G2, C2, and H2 (Figs. 1b (left) and 1c), and C and F (Fig. 1b (right)). The calculations of the flow around a sharp double cone were carried out according to two computation schemes (Fig. 1b): with a section of an undisturbed oncoming flow and without such a section.

3. METHOD OF NUMERICAL INTEGRATION

As already noted, the PERAT-2D computer code is a simplified version of the NERAT-2D code. The main changes concerned the transition to the perfect gas model and, thereby, significant savings in memory used (without using multi-block parallel computing technology). The numerical algorithm of calculations remained the same.

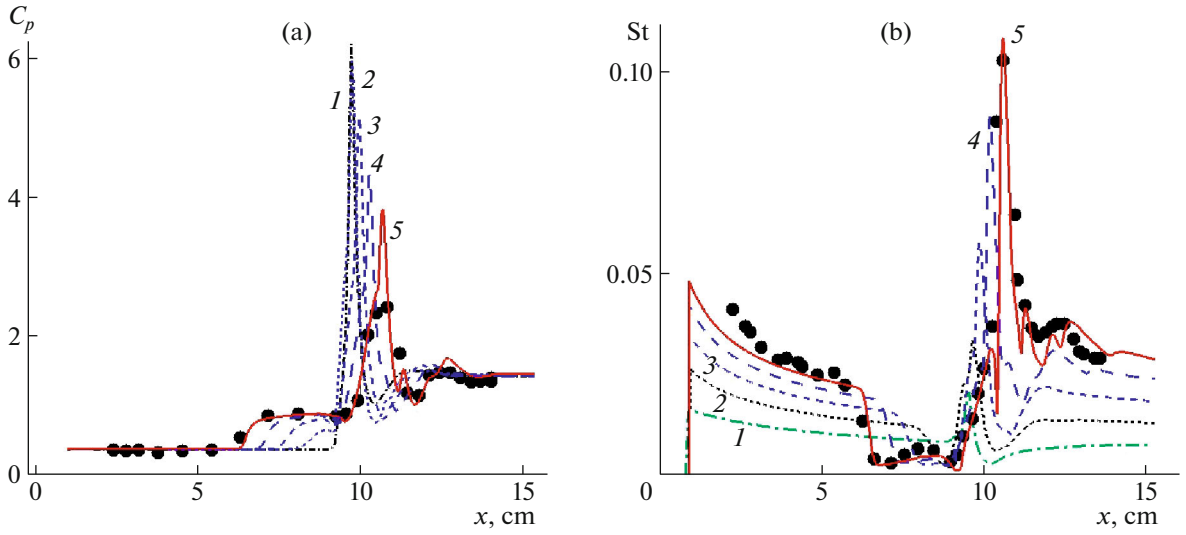

Fig. 3. Distribution of the (a) pressure and (b) heat transfer coefficient in the flow around a double blunt cone in the Run#35a experiment: (*1*–*5*) computed on grids (*1*) 251 × 25 (along and across the surface), (*2*) 501 × 49, (*3*) 1001 × 97, (*4*) 2002 × 193, and (*5*) 4001 × 385; and (dots) experimental data [1].

System of equations (1)–(4) was integrated up to the convergence of the sought grid solutions with an accuracy of 10^{-4}. The relative calculation error of each function was determined over the entire flow field. The gas-dynamics equations (continuity equation and two Navier–Stokes equations) were integrated using the AUSM second-order finite difference scheme [30]. The heat equation was integrated using an implicit finite-difference scheme of the second order of accuracy in space and time. The use of implicit finite difference schemes for solving the heat equation significantly increased the efficiency of the computational procedure. It should be emphasized that additional numerical constraints and any kind of artificial viscosity were not used.

4. RESULTS OF NUMERICAL SIMULATION

The initial data for the calculations performed are given in Table 1. This paper presents the calculation results for a hollow skirted cylinder (options Run#11 and Run#14), a pointed double cone (Run#35a), and a blunt double cone (Run#31 and Run#32).

Before discussing the results of validating calculations, we emphasize the strong influence of the finite difference schemes used for all calculated options, without exception. The choice and shape of the outer boundary of the computational domain turned out to be quite important (Fig. 1).

Figure 3 shows the distributions of pressure and heat transfer coefficients for the Run#35 experiment, obtained using finite difference grids of various sizes. These are typical results for all calculated variants in terms of the influence of grid details on the agreement between the calculated and experimental data.

The distributions of gas-dynamic functions in the experiment with a flow around a hollow skirted cylinder (Run#11a) are shown in Figs. 4 and 5. The calculations took into account the region of undisturbed flow up to the front edge of the hollow cylinder.

Let us note the main features of the flow field. The shock wave generated by the front edge of the cylinder interacts with the boundary layer at a distance $x \sim 15.5$ cm. Near the outer surface of the hollow cylinder, a boundary layer is formed, which is separated from the bow shock wave by an inviscid flow region. The boundary layer develops from the edge along the surface of the cylinder until it reaches the region of reverse eddy gas motion in the zone of flow separation near the bend in the generatrix.

The existence of a separated flow region above the kink of the generatrix is an important feature of the interaction of a shock wave with a boundary layer above a conical skirt. Here, an area of increased pressure arises, which caused the turn of the flow in the boundary layer towards the main flow. It can be seen from Fig. 4b that the region of increased pressure propagates from the point of interaction of the shock wave with the boundary layer ($x \sim 15.5$ cm) against the flow to a distance $x \sim 9$ cm, where the region of reverse motion ends. The reverse motion zone is clearly seen in Fig. 4d.

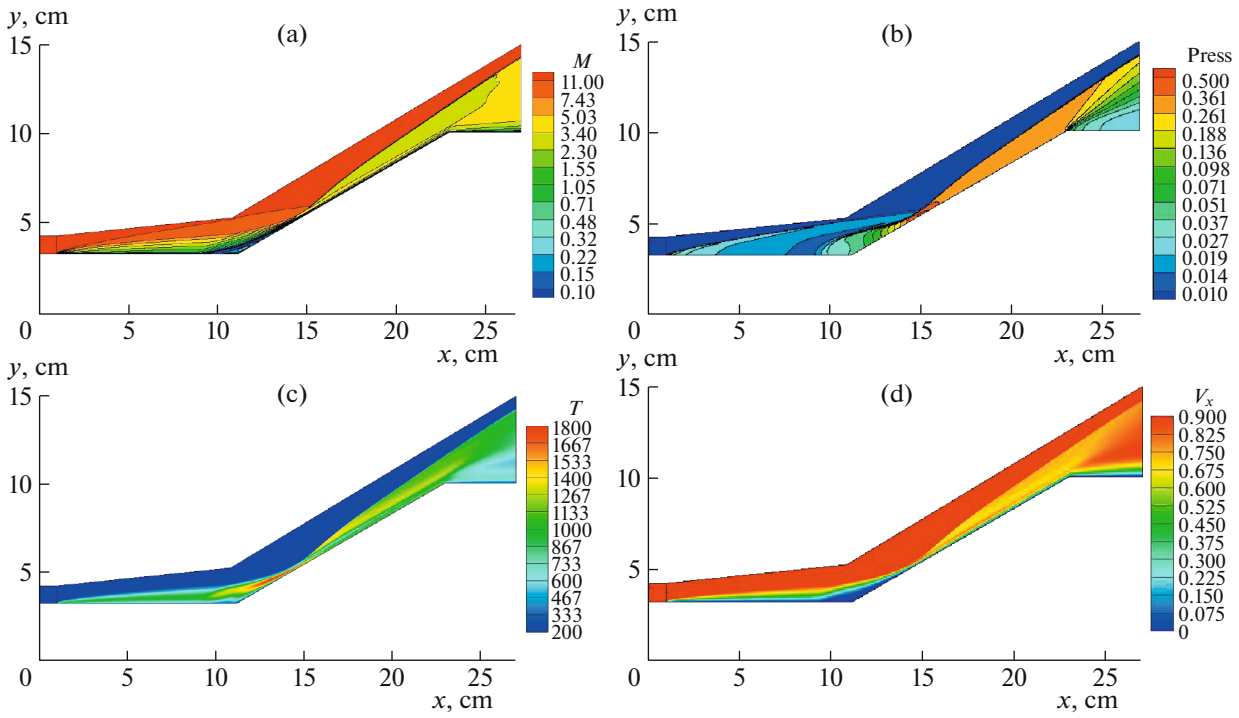

Fig. 4. Field of (a) Mach numbers, (b) pressure (Pres = $p/\rho_\infty V_\infty^2$), (c) temperature (in K), and (d) longitudinal velocity $V_x = u/V_\infty$ for Run#11a test problem (computational grid 703 × 1505, factor of grid refinement to the surface $\beta = 0.8$).

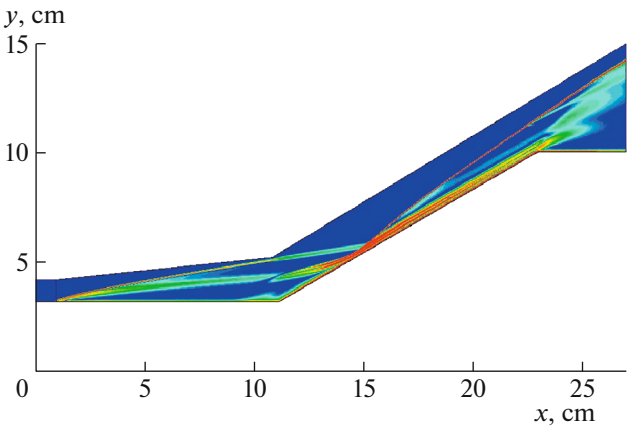

Fig. 5. Density gradient modulus field for Run#11a test problem (computational grid 703 × 1505, factor of grid refinement to the surface $\beta = 0.8$).

A lot of information on the flow structure can be obtained from the analysis of the density gradient modulus field in Fig. 5. Here, we clearly see the outer and near-wall regions of the boundary layer on the outer surface of the cylinder and the front of the bow shock wave. Above the conical skirt, there are shocks of the reflected wave, a shock of the separation zone, shocks of reattachment, and a boundary layer.

Noteworthy is the zone of elevated temperature ($12 \le x \le 15$ cm) formed above the separated flow and the region with elevated temperature behind the reflected shock wave.

Figure 6 shows the distributions of pressure and density of the convective heat flux along the surface for the nominal speed of oncoming flow $V_\infty = 2.6$ km/s (a), as well as for reduced ($V_\infty = 2.2$ km/s) (b), and increased speed ($V_\infty = 2.8$ km/s) (c). These calculations were performed in order to estimate the effect of possible inhomogeneity in the oncoming flow.

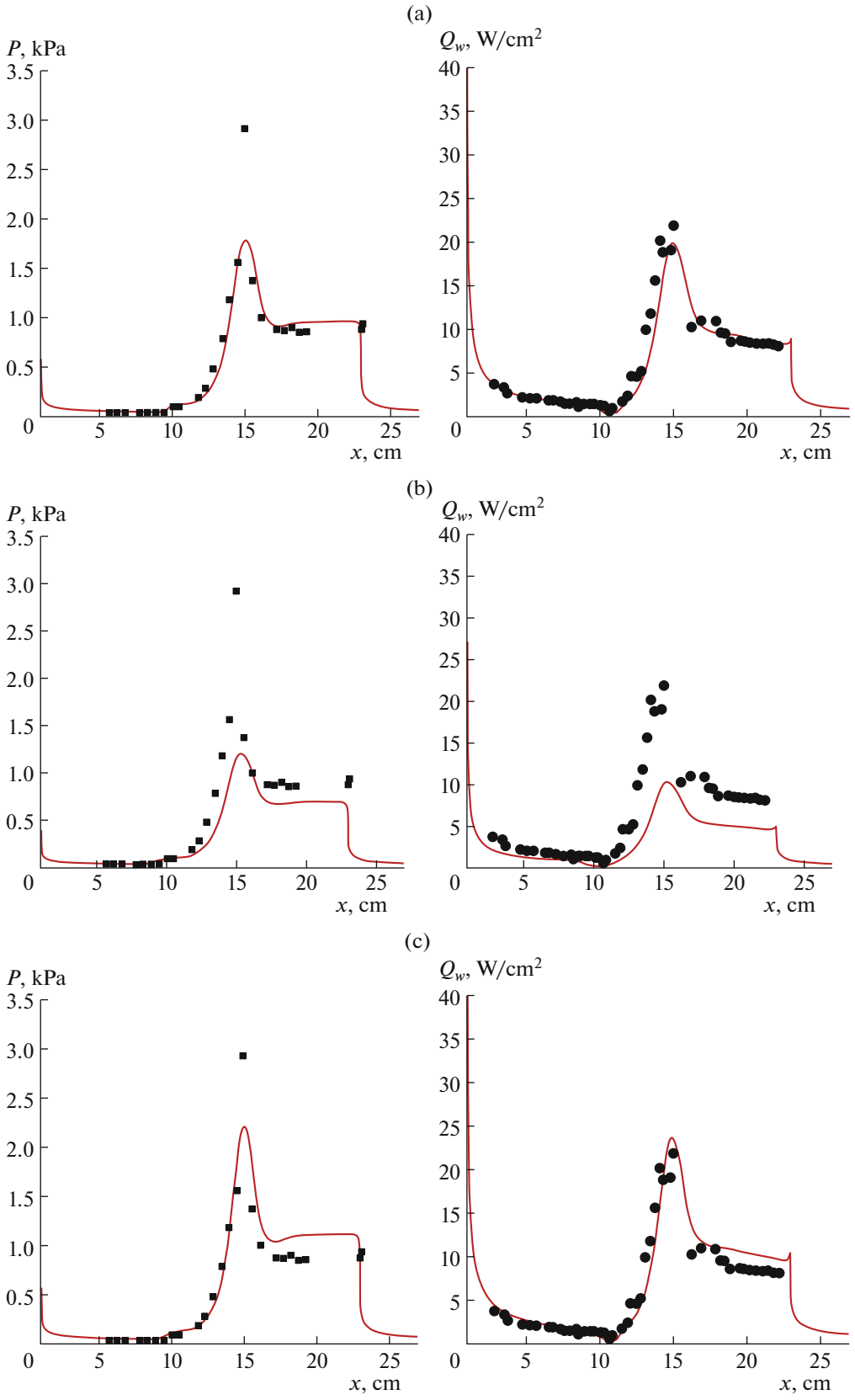

Fig. 6. Distribution of (left) pressure and (right) density of the convective heat flux along the surface of a hollow skirted cylinder for Run#11a test problem (computational grid 703 × 1505: (a) V_∞ = 2.6, (b) 2.2, and (c) 2.8 km/s).

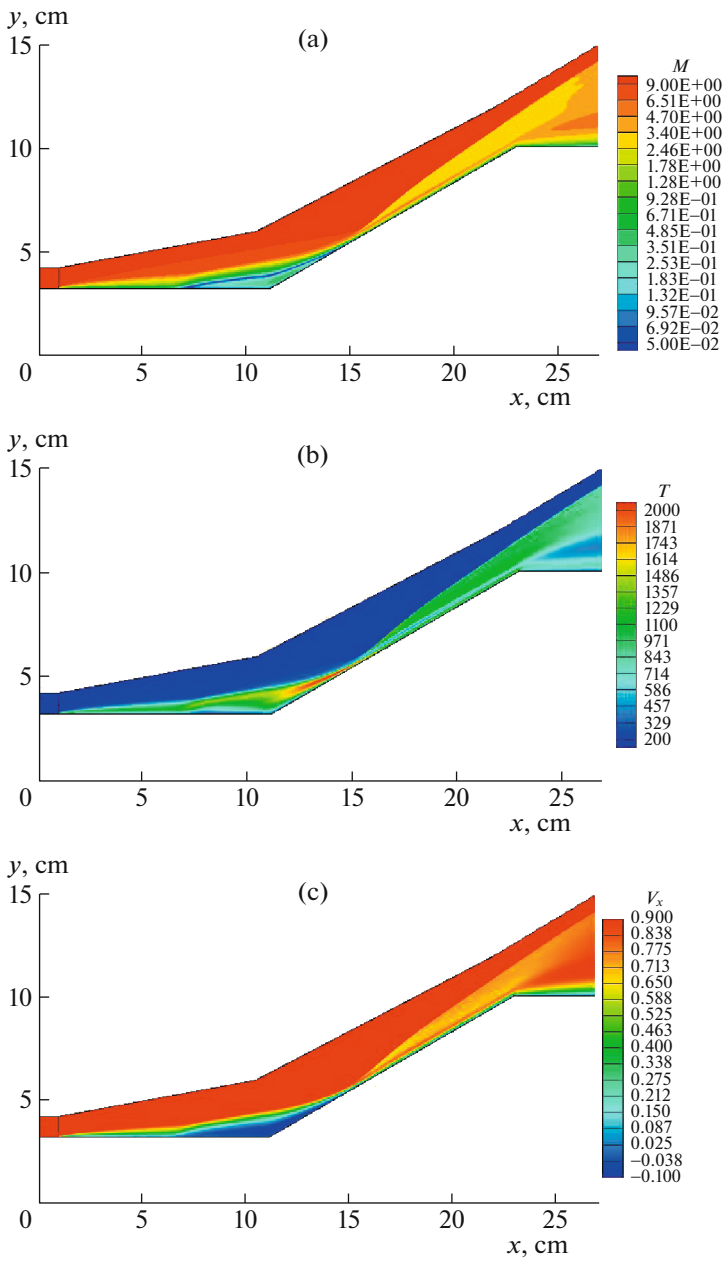

Fig. 7. Field of (a) Mach numbers, (b) temperature (in K), and (c) longitudinal velocity $V_x = u/V_\infty$ for Run#14a test problem (computational grid 703 × 1505, factor of grid refinement to the surface $\beta = 0.8$).

A change in the speed of the oncoming flow leads to a regular decrease (with a decrease in V_∞) or an increase in pressure and heat flux on the surface of the skirt. For all calculated variants, there is a noticeable difference in pressure at the point of interaction of the incident shock wave with the boundary layer (at $x \sim 15$ cm). In the papers of other authors, such a discrepancy is also observed.

On the whole, it should be noted that the local increase in pressure in the separated flow zone and above the skirt surface is in good agreement with the experimental values at the nominal speed of the oncoming flow.

The heat flux density distribution also correlates well with the experimental data, including the entropy flow zone ($x \sim 11$ cm), where a local decrease in the heat flux density is noticeable.

Figures 7–9 present the results of calculating the flow around a hollow cylinder with a conical skirt for the Run#14a test. The difference from the previously considered variant is an increase in the density and

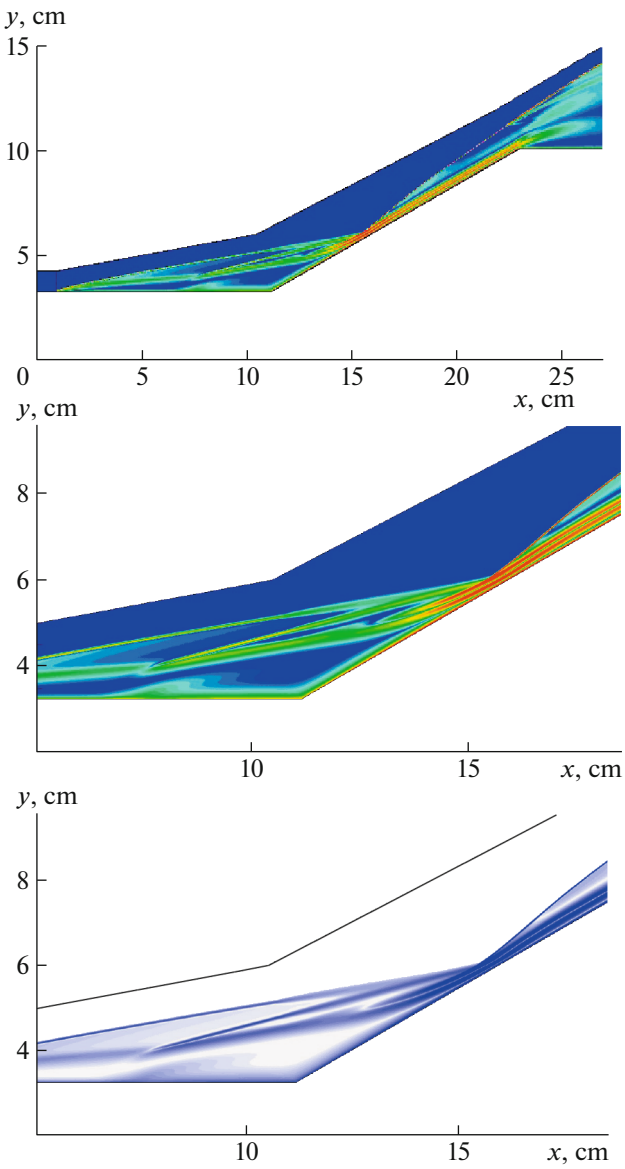

Fig. 8. Density gradient modulus field for Run#14a test problem (computational grid 703 × 1505, factor of grid refinement to the surface $\beta = 0.8$).

pressure in the oncoming flow with a slight decrease in speed, which leads to a decrease in the Mach number to M ~ 10.

In general, the flow field structure turns out to be similar to that shown above; however, noteworthy is a much more extended region of the separated flow above the kink of the generatrix. It can be seen in Fig. 9 that the length of the region of reduced pressure and increased convective heat flux density associated with the zone of separated flow is about 5 cm. The agreement with the experimental data is quite good, except for the maximum value of the heat flux density. Note that, in the previous variant, a similar discrepancy was observed for the maximum pressure.

It is worth noting once more the feature of the flow field structure in the Run#14 test problem. Since the size of the separation zone has become larger, a viscous interaction of the separation shock with the separation zone is observed, such that the indicated separation shock reaches the bow shock wave earlier than the interaction of the bow shock with the boundary layer on the conical skirt occurs.

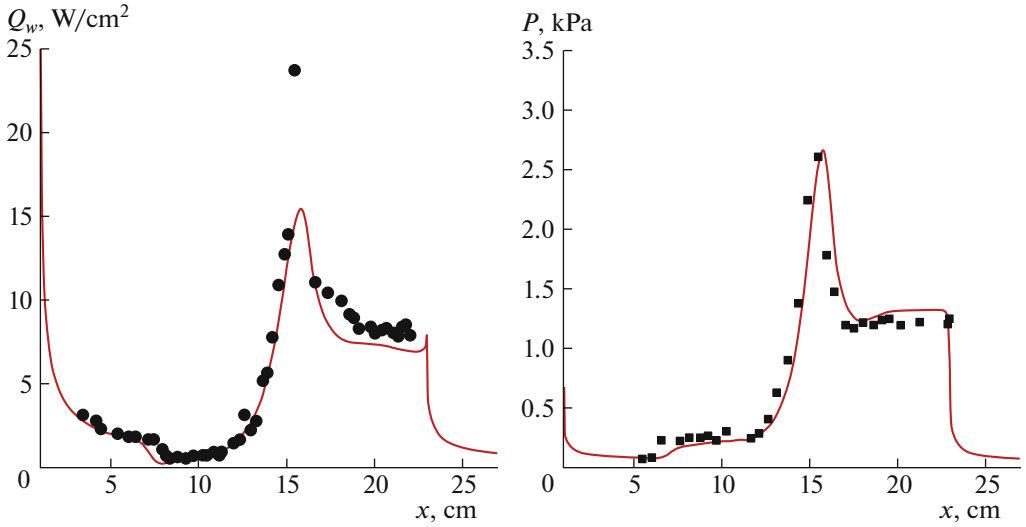

Fig. 9. Distribution of the convective heat flux density and pressure along the surface of a hollow skirted cylinder for Run#14a test problem.

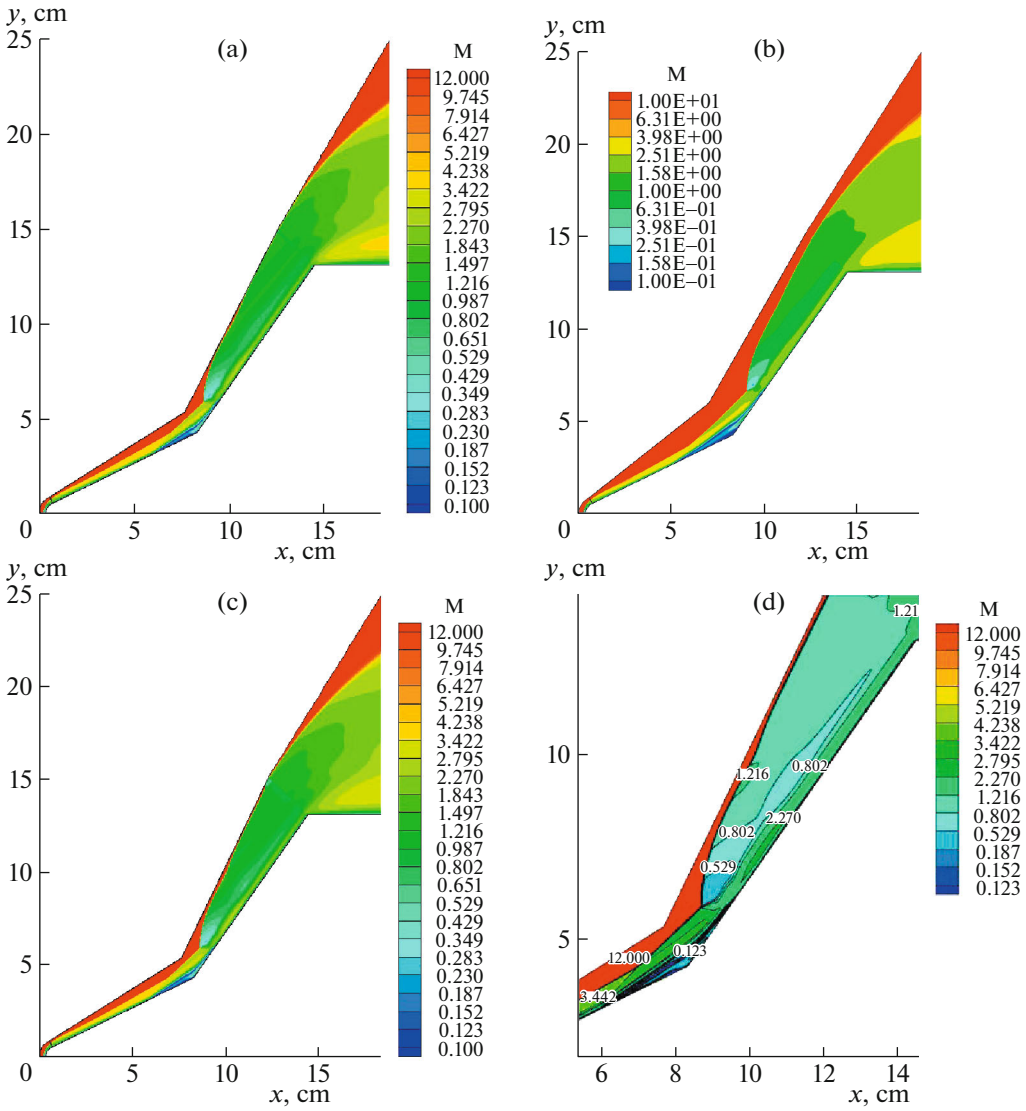

Fig. 10. Mach number field for Run#31 test problem (computational grid 703 × 1505, factor of grid refinement to the surface $\beta = 0.7$ (a), 0.6 (b), and 0.3 (c, d)).

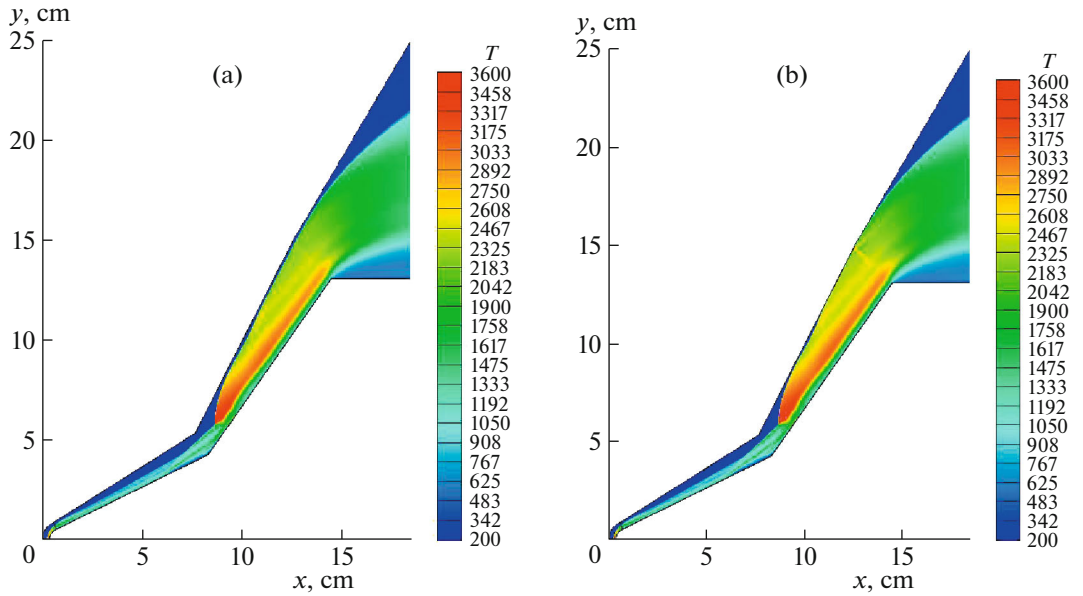

Fig. 11. Temperature field (in K) for Run#31a test problem (computational grid 703 × 1505, factor of grid refinement to the surface $\beta = 0.8$ (a) and (b) 0.7).

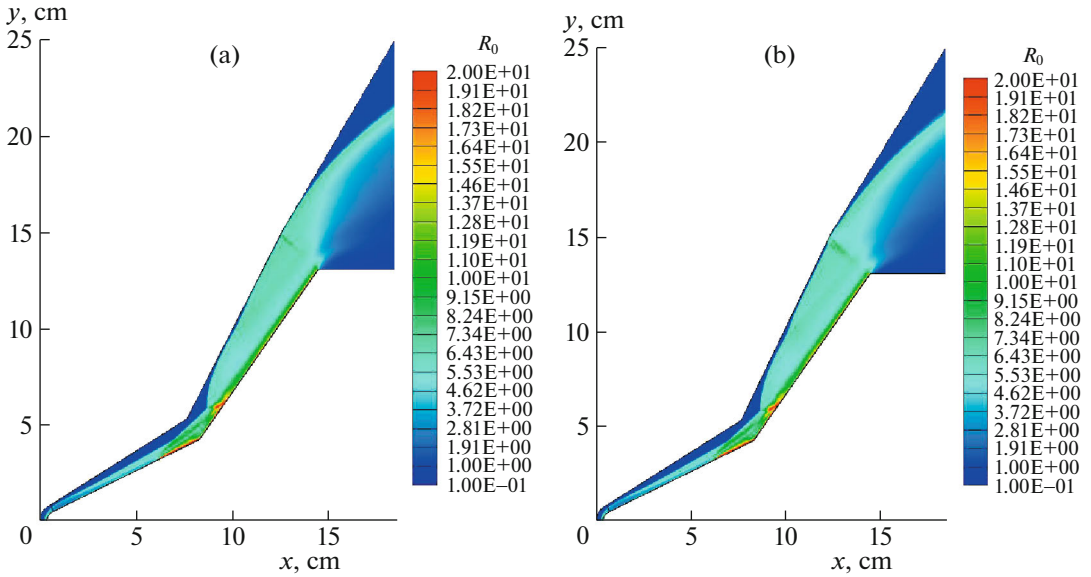

Fig. 12. Density field $R_0 = \rho/\rho_\infty$ for Run#31 test problem (computational grid 703 × 1505, factor of grid refinement to the surface $\beta = 0.7$ (a) and (b) 0.3).

In the Run#31 test variant, the interaction of a shock wave with a boundary layer near the surface of a blunt double cone is studied in which the influence of the entropy layer formed in the flow around the head bluntness is also manifested.

Figures 10–13 show the profiles of gas-dynamic functions obtained at different refining of the computational grid to the cone surface and the configuration of the outer boundary of the computational domain. The profiles shown give an idea of the degree of its effect. Visually, the flow field structure remains practically unchanged. However, the influence of pressure and density distribution of the convective heat flux is very noticeable, which is manifested when compared with experimental data.

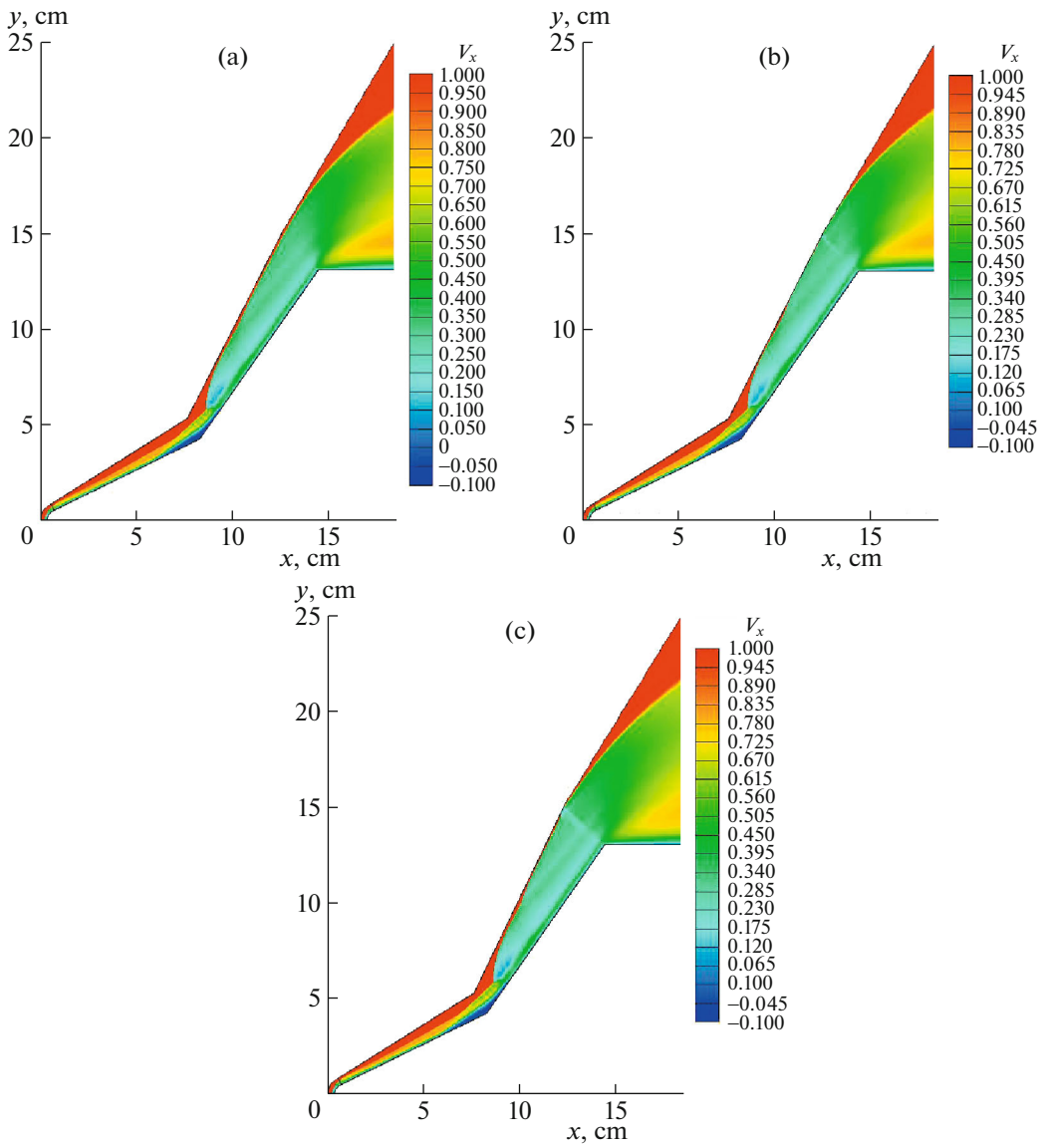

Fig. 13. Longitudinal velocity field $V_x = u/V_\infty$ for Run#31 test problem (computational grid 703 × 1505, factor of grid refinement to the surface β = 0.8 (a), 0.7 (b), and 0.3 (c)).

It is worth noting the specificity of the flow around a double blunt cone. Firstly, this is the formation of an entropy layer from the bluntness of the cone. This is clearly seen in the distributions of temperature (Fig. 11) and the density gradient modulus (Fig. 14). The boundary of the entropy layer is also clearly seen in Fig. 14 (curve departing from the bow shock wave). The boundary of the entropy layer extends up to the shock generated by the separated flow.

An important feature of the test problem under consideration is a much more complex flow structure in the region of interaction of the bow shock wave with the boundary layer ($x \sim 9$–10 cm). Note the curvature of the bow shock wave under the action of the separation shock (Fig. 14).

Behind the interaction region, noteworthy is the zone of subsonic motion behind the front of the reflected bow shock wave. Below this zone, there is a subregion of supersonic motion and, closer to the surface, the boundary layer region (see Fig. 10).

A remarkable element of the flow is the high-temperature region of subsonic motion, where the temperature reaches about 3000 K (see Fig. 11). Near the surface of the double cone, we note two zones of increased density: in the region of interaction of the incident shock wave with the boundary layer and in the region of the separated flow (see Fig. 12).

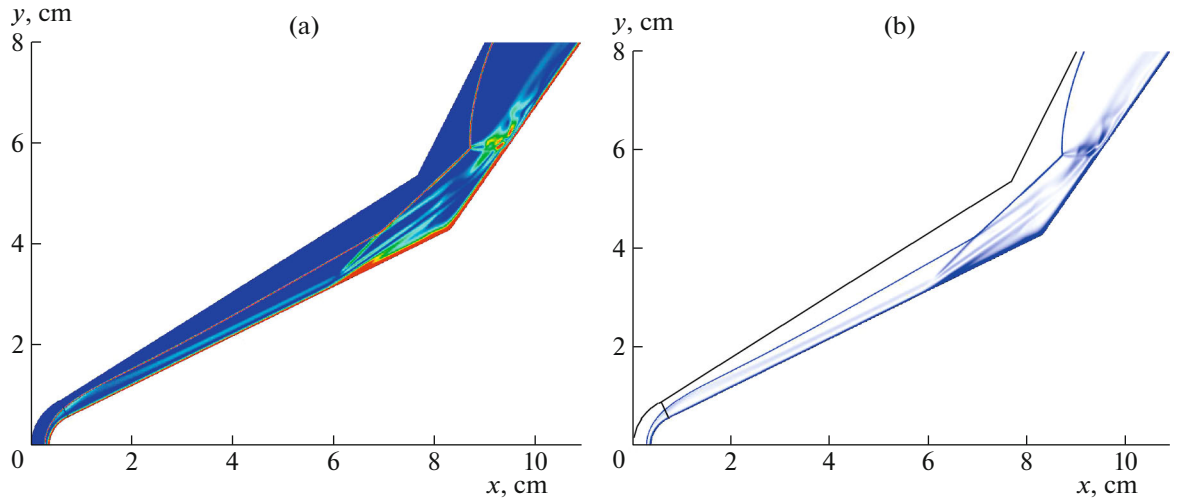

Fig. 14. Density gradient modulus field for Run#31 test problem (computational grid 703 × 1505, factor of grid refinement to the surface β = 0.7).

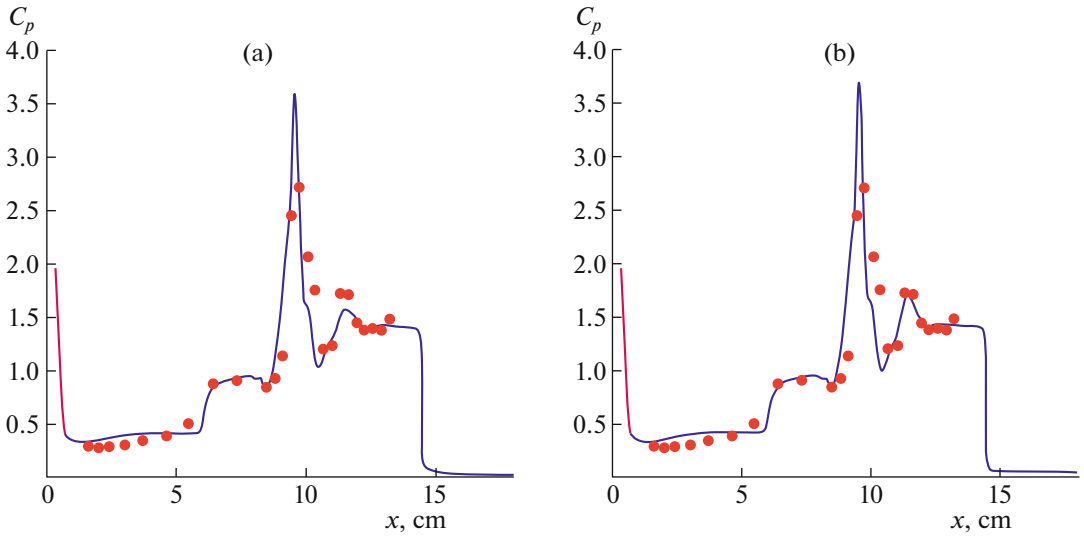

Fig. 15. Distribution of the pressure coefficient along the surface of a skirted hollow cylinder for Run#31 test problem (computational grid 703 × 1505, factor of grid refinement to the surface β = 0.7 (a) and 0.3 (b)).

Figure 13 shows the longitudinal velocity distributions for three degrees of refinement of the computational grid to the surface. The position of the outer boundary of the computational domain was carefully chosen in numerical experiments to avoid the influence on the solution.

Despite the smallness of the visible differences in the velocity profiles, it should be noted that such differences are visible on the distributions of the pressure and heat transfer coefficients in comparison with the experimental data (Figs. 15 and 16).

Figure 17 shows the calculation results for the Run#32 test variant, which differs from the previous one in flow velocity, which is reduced to $M = 10.6$. The pressure in the oncoming flow is about twice as high.

The features of the flow remain similar to the previous test case. However, the region of the separated flow here is more extended (compare Figs. 16 and 19).

In Fig. 17a, we can clearly see the zone of increased pressure in the region of interaction of the bow shock wave with the boundary layer (at $x \sim 10$ cm) and the zone of increased pressure above the separated

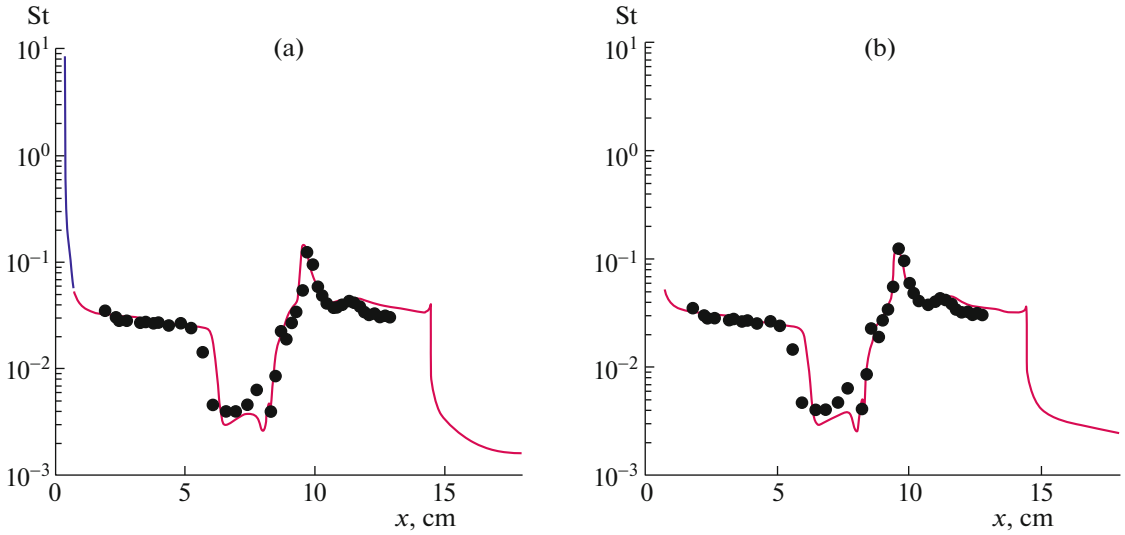

Fig. 16. Distribution of the heat transfer coefficient St along the surface of a hollow skirt cylinder for Run#31 test problem (computational grid 703 × 1505, factor of grid refinement to the surface β = 0.7 (a) and 0.3 (b)).

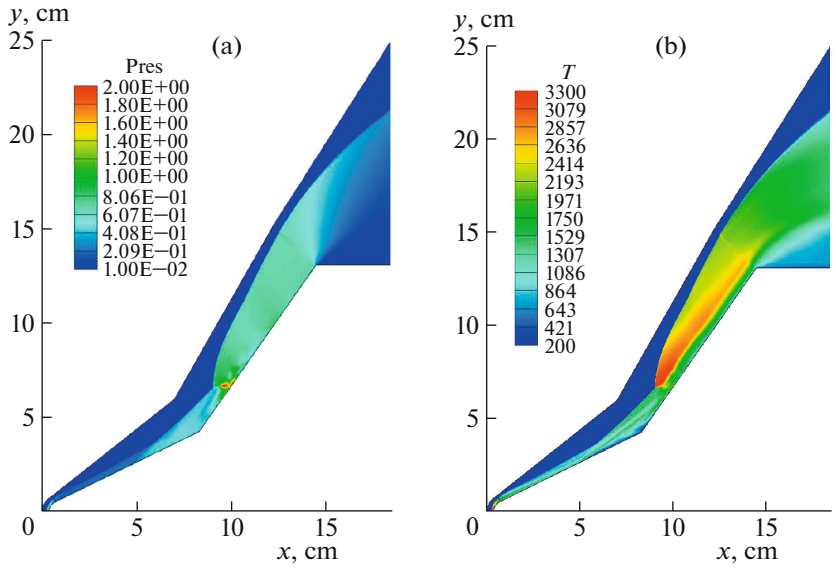

Fig. 17. Pressure (Pres $= p/\rho_\infty V_\infty^2$) and temperature (in K) field for Run#32 test problem (computational grid 703 × 1505, factor of grid refinement to the surface β = 0.6).

flow. The enlarged region of the separated flow leads to a noticeably earlier deviation of the bow shock wave from the cone surface (Fig. 18). Near the surface, several regions of super- and subsonic motion are observed. Near the front bluntness, a region of subsonic motion is formed. Another subsonic zone is formed in the separated flow region. The subsonic zone is observed behind the reflected shock wave after interaction with the boundary layer. Finally, subsonic flow takes place in the boundary layer along the entire surface.

The test variant considered turned out to be very difficult for a successful description of the experimental data. As can be seen in Fig. 19, in the calculations, a somewhat smaller extent of the separated flow zone is obtained.

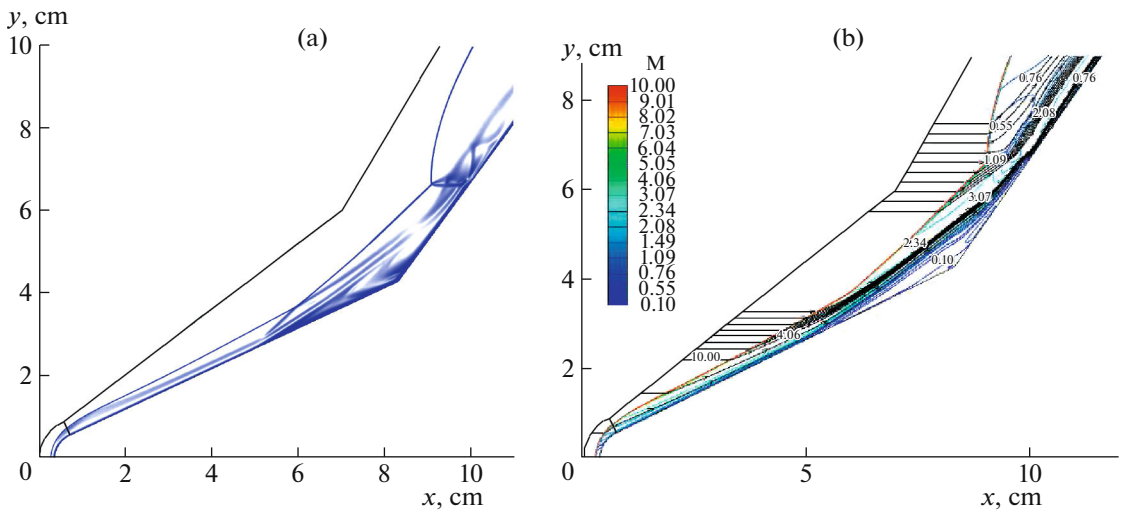

Fig. 18. Field of (a) density gradient modulus and (b) Mach numbers for Run#32 test problem (computational grid 703 × 1505, factor of grid refinement to the surface β = 0.6).

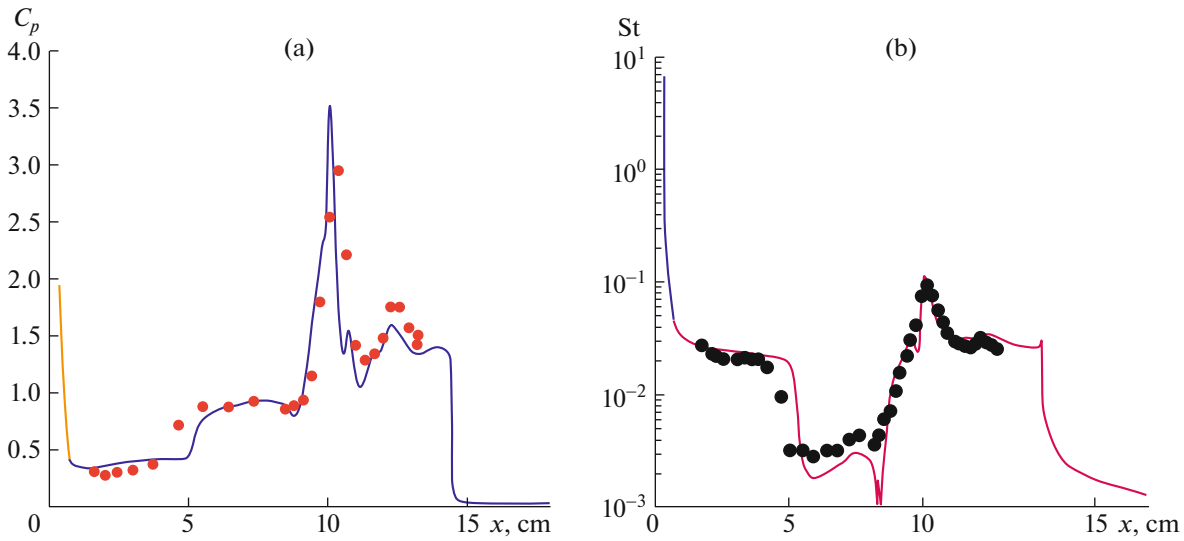

Fig. 19. Distributions of the (a) pressure (C_p) and (b) heat (St) transfer coefficients along the surface of a double blunt cone for Run#32 test problem (computational grid 703 × 1505, factor of grid refinement to the surface β = 0.6).

In the Run#35a test problem (Figs. 20–22), we studied the flow around a double sharp cone. The structure of the flow field as a whole is similar to that considered above, but the absence of an entropy layer makes all shocks and transition zones more distinct.

Figure 20 shows distributions of gas-dynamic functions for the Run#35 test problem, and Fig. 21 shows the modulus of the density gradient and Mach numbers with streamlines. The regions of super- and subsonic motion are also clearly visible here. Figure 22 demonstrates good agreement between the calculated and experimental data.

CONCLUSIONS

Using the author's PERAT-2D computer code, validation calculations of the shock-wave interaction with a laminar boundary layer in a hypersonic flow around a hollow cylinder with a conical skirt and a sharp and blunt double cone have been performed.

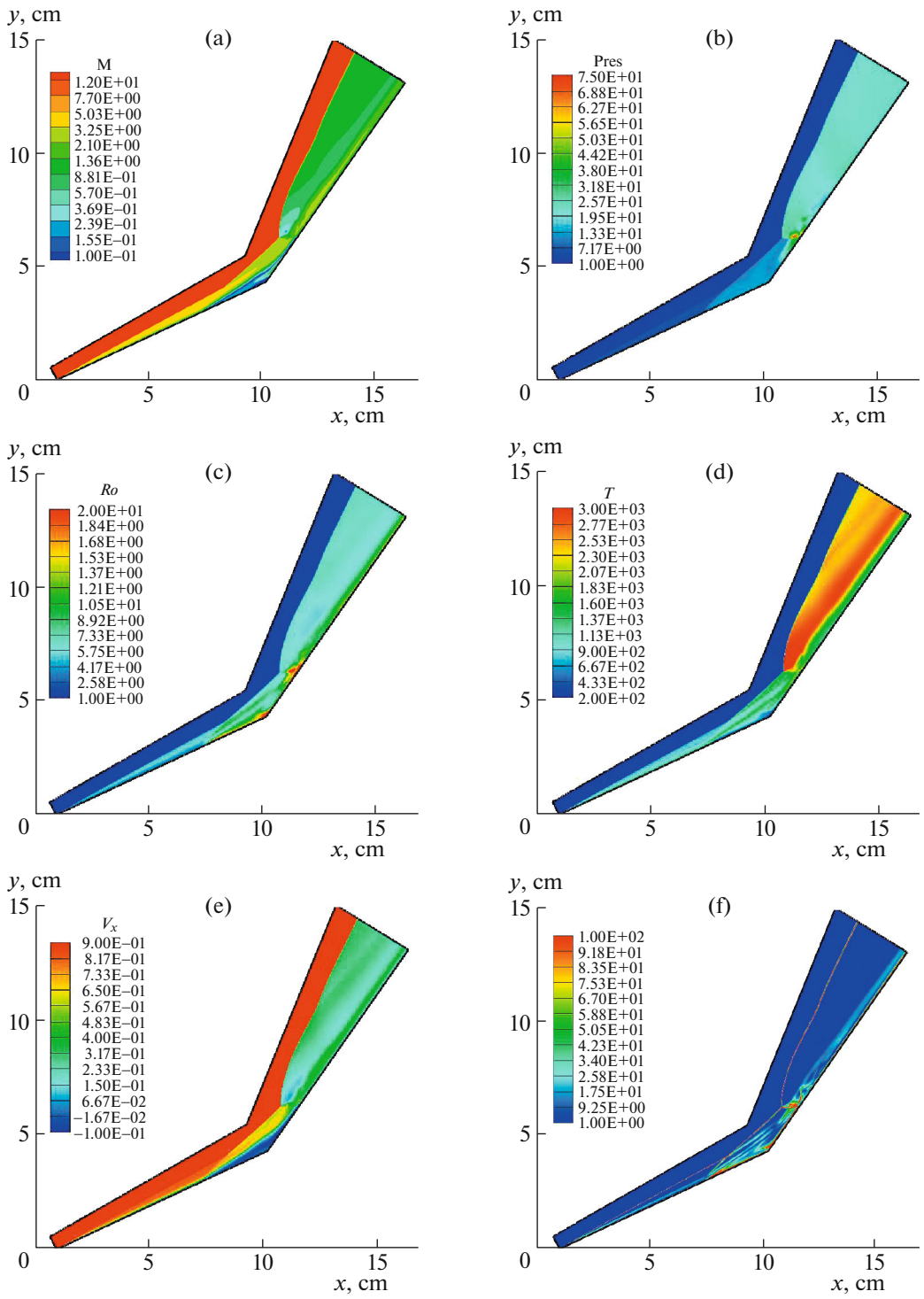

Fig. 20. Field of (a) Mach numbers, (b) pressure (Pres= $p/\rho_\infty V_\infty^2$), (c) density, (d) temperature (in K), (e) longitudinal velocity $V_x = u/V_\infty$, and (f) density gradient modulus for Run#35a test problem (computational grid 385 × 4001, factor of grid refinement to the surface $\beta = 0.6$).

The experimental data obtained in Run#11, 14, 31, 32, and 35 experiments at the CUBRC hypersonic wind tunnel [1] were studied using numerical simulation.

Good agreement is shown with the experimental data on the distribution of pressure and density of the convective heat flux along the surface of the models.

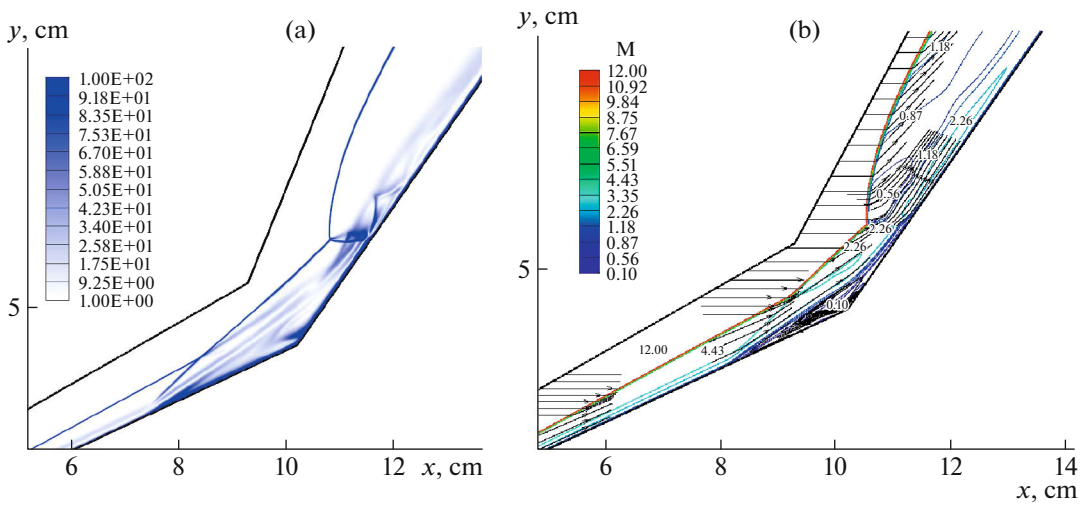

Fig. 21. Fields of the (a) density gradient modulus and (b) Mach numbers for Run#35a test problem (computational grid 385 × 4001, factor of grid refinement to the surface β = 0.6).

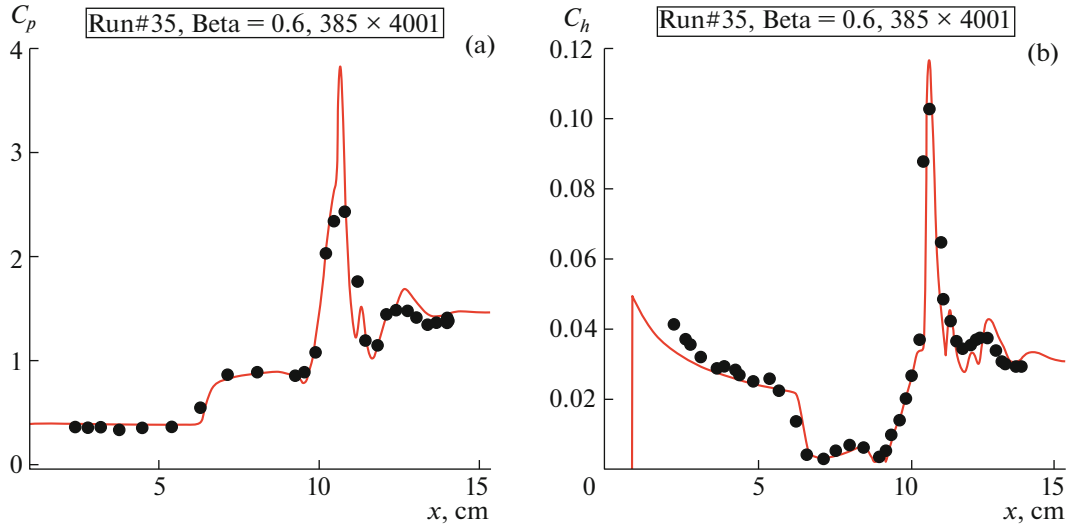

Fig. 22. Distributions of the (a) pressure (C_p) and (b) heat (C_h) transfer coefficients along the surface of a double sharp cone for Run#35a test problem.

In the numerical experiments, the influence of the calculated parameters and the geometry of the computational domain on the degree of agreement with the experimental data was studied. It has been shown that, for good quantitative agreement between the calculated and experimental data when using second-order schemes implemented for the PERAT-2D code, very detailed computational grids are required, which, in addition to a good description of the experimental data, allow one to obtain detailed resolution of the gas-dynamic structure of the flow in shock-wave interaction with the boundary layer in a hypersonic flow.

FUNDING

This study was carried out within a state task for the Russian Academy of Sciences (state registration no. AAAA-A20-120011690135-5).

CONFLICT OF INTEREST

The author declares that he has no conflicts of interest.

REFERENCES

1. Holden, M.S., Wadhams, T.P., Harvey, J.K., and Candler, G.V., Comparison between measurements in regions of laminar shock wave boundary layer interaction in hypersonic flows with Navier–Stokes and DSMC solutions, *Report no.* RTO-TR-AVT-007-03.
2. Candler, G.V., Nompelis, I., Druguet, M.-C., Holden, M.S., Wadhams, T.P., and Boyd, I.D., CFD validation for hypersonic flight: hypersonic double-cone flow simulation, *Proc. 40th AIAA Aerospace Sciences Meeting & Exhibition,* Reno, NV, 2002, paper no. AIAA 2002-0581.
3. MacLean, M. and Holden, M., Validation and comparison of WIND and DPLR results for hypersonic, laminar problems, *Proc. 42th AIAA Aerospace Sciences Meeting & Exhibition,* Reno, NV, 2004, paper no. AIAA 2004-0529.
4. Moss, J.N. and Olejniczak, J., Shock-wave/boundary-layer interactions in hypersonic low density flows, *Proc. 7th AIAA/ASME Joint Thermophysics and Heat Transfer Conf.,* Albuquerque, NM, 1998, paper no. AIAA 98-2668.
5. Wright, M.J., Sinha, K., Olejniczak, J., and Candler, G.V., Numerical and experimental investigation of double-cone shock interactions, *AIAA J.,* 2000, vol. 38, no. 12, pp. 2268–2276. https://doi.org/10.2514/2.918
6. Harvey, J.K., Holden, M.S., and Wadhams, T.P., Code validation study of laminar shock/boundary layer and shock/shock interactions in hypersonic flow, *Proc. 39th Aerospace Sciences Meeting and Exhibition,* Reno, NV, 2001, paper no. AIAA 2001-1031.
7. Wang, W.-L. and Boyd, I.D., Particle and continuum computations of hypersonic flow over sharp and blunted cones, *Proc. 35th AIAA Thermophysics Conf.,* Anaheim, CA, 2001, paper no. AIAA 2001-2900.
8. Kato, H. and Tannehill, J.C., Computation of hypersonic laminar separated flows using an iterated PNS algorithm, *Proc. 39th Aerospace Sciences Meeting & Exhibition,* Reno, NV, 2001, paper no. AIAA 2001-1028.
9. Candler, G.V. and Druguet, M.-C., Navier–Stokes predictions of hypersonic double-cone and cylinder-flare flow fields, *Proc. 39th Aerospace Sciences Meeting & Exhibition,* Reno, NV, 2001, paper no. AIAA 2001-1024.
10. Gnoffo, P.A., CFD validation studies for hypersonic flow prediction, *Proc. 39th Aerospace Sciences Meeting & Exhibition,* Reno, NV, 2001, paper no. AIAA 2001-1025.
11. Roy, C.J., Gallis, M.A., Bartel, T.J., and Payne, J.L., Navier–Stokes and DSMC simulations for hypersonic laminar shock-shock interaction flows, *Proc. 40th AIAA Aerospace Sciences Meeting & Exhibition,* Reno, NV, 2002, paper no. AIAA 2002-0737.
12. Harvey, J.K., Holden, M.S., and Candler, G.V., Validation of DSNC/Navier–Stokes computations for laminar shock wave/boundary layer interactions in hypersonic flows, *AIP Proc.,* 2003, vol. 663, pp. 417–424.
13. Moss, J.N. and Bird, G.A., DSMC simulations of hypersonic flows with shock interactions and validation with experiments, *Proc. 37th AIAA Thermophysics Conf.,* Portland, 2004, paper no. AIAA 2004-2585.
14. Candler, G. and Holden, M., Numerical evaluation of flow conditions in the LENS reflected shock-tunnel facilities, *Proc. 43rd AIAA Aerospace Sciences Meeting,* Reno, NV, 2005, paper no. AIAA 2005-0903.
15. Knight, D., RTO WG 10: test cases for CFD validation of hypersonic flight, *Proc. 40th AIAA Aerospace Sciences Meeting & Exhibition,* Reno, NV, 2002, paper no. RTO-TR-AVT-007-V3.
16. MacLean, M., Holden, M., Wadhams, T., and Parker, R., A computational analysis of thermochemical studies in the LENA facilities, *Proc. 45th AIAA Aerospace Sciences Meeting & Exhibition,* Reno, NV, 2007, paper no. AIAA 2007-0121.
17. MacLean, M., Mundy, E., Wadhams, T., Holden, M., Johnson, H., and Candler, G., Comparisons of transition prediction using PSE-Chem to measurements for a shock tunnel environment, *Proc. 37th AIAA Fluid Dynamics Conf. and Exhibition,* Miami, 2007, paper no. AIAA 2007-4490.
18. Shen, Y., Zha, G., Huerta, M.A., and Gables, C., Simulation of hypersonic shock wave/boundary layer interaction using high order WENO scheme, *Proc. 48th AIAA Aerospace Sciences Meeting Including the New Horizons Forum and Aerospace Exposition,* Orlando, 2010, paper no. AIAA 2010-1047.
19. Holden, M., MacLean, M., Wadhams, T., and Mundy, E., Experimental studies of shock wave/turbulent boundary layer interactions in high Reynolds number supersonic and hypersonic flows to evaluate the performance of CFD codes, *Proc. 40th Fluid Dynamics Conf. and Exhibition,* Chicago, 2010, paper no. AIAA 2010-4468.
20. Jing, L., Hong, X., and Di, W., Simulation and experimental validation of hypersonic shock wave interaction, *Res. J. Appl. Sci., Eng. Technol.,* 2013, vol. 6, no. 22, pp. 4221–4224.
21. Hao, J., Wang, J., and Lee, C., Numerical simulation of high-enthalpy double-cone flows, *AIAA J.,* 2017, vol. 55, no. 5, pp. 2471–2475. https://doi.org/10.2514/1.J056643

22. Walker, S. and Schmisseur, J.D., CFD validation of shock-shock interaction flow fields, *Proc. 40th AIAA Aerospace Sciences Meeting & Exhibition,* Reno, NV, 2002, paper no. AIAA 2002-0436.
23. Candler, G.V. and Nompelis, I., CFD validation for hypersonic flight: real gas flows, *Proc. 40th AIAA Aerospace Sciences Meeting & Exhibition,* Reno, NV, 2002, paper no. AIAA 2002-0434.
24. Knight, D., Hong, Y., Panaras, A., and Zheltovodov, A., RTO WG 10: CFD validation for shock wave turbulent boundary layer interactions, *Proc. 40th AIAA Aerospace Sciences Meeting & Exhibition,* Reno, NV, 2002, paper no. AIAA 2002-0437.
25. Holden, M., MacLean, M., Wadhams, T., and Dufrene, A., Measurements of real gas effects on regions of laminar shock wave/boundary layer interaction in hypervelocity flows for "blind" code validation studies, *Proc. 21st AIAA Computational Fluid Dynamics Conf.,* San Diego, 2013, paper no. AIAA 2013-2837.
26. Borovoi, V.Ya., Egorov, I.V., Mosharov, V.E., Skuratov, A.S., and Radchenko, V.N., *Ekstremal'nyi nagrev tel v giperzvukovom potoke* (Extreme Heating for Bodies in Hypersonic Flow), Moscow: Nauka, 2018.
27. Borovoy, V.Ya., Skuratov, A.S., and Struminskaya, I.V., On the existence of a threshold value of the plate bluntness in the interference of an oblique shock with boundary and entropy layers, *Fluid Dyn.,* 2008, vol. 43, no. 3, pp. 369–380.
28. Borovoi, V.Ya., Egorov, I.V., Skuratov, A.S., and Struminskaya, I.V., Laminar heat exchange on sharp and blunt plates in a hypersonic air flow, *Fluid Dyn.,* 2005, vol. 40, no. 1, pp. 148–158.
29. Shang, J.S. and Surzhikov, S.T., Magnetoaerodynamic actuator for hypersonic flow control, *AIAA J.,* 2005, vol. 43, no. 8, pp. 1633–1643.
30. Edwards, J.R. and Liou, M.-S., Low-diffusion flux-splitting methods for flow at all speeds, *AIAA J.,* 1998, vol. 36, no. 9, pp. 1610–1617.

Translated by E. Chernokozhin